Probing Structural and Magnetic Instabilities and Hysteresis in Heuslers by Density Functional Theory Calculations

Peter Entel,* Markus E. Gruner, Sebastian Fähler, Mehmet Acet, Asli Çahır, Raymundo Arróyave, Sanjubala Sahoo, Thien C. Duong, Anjana Talapatra, Leonid Sandratskii, Sergei Mankowsky, Tino Gottschall, Oliver Gutfleisch, Patricia Lázpita, Volodymyr A. Chernenko, Jose M. Barandiaran, Vladimir V. Sokolovskiy, and Vasiliy D. Buchelnikov

Martensitic transformations of rapidly quenched and less rapidly cooled Heusler alloys of type Ni–Mn–X with X = Ga, In, and Sn are investigated by *ab initio* calculatioms. For the rapidly cooled alloys, we obtain the magnetocaloric properties near the magnetocaloric transition. For the less rapidly quenched alloys these magnetocaloric properties start to change considerably, each alloy transforms during temper-annealing into a dual-phase composite alloy. The two phases are identified to be cubic Ni–Mn–X and tetragonal NiMn.

1. Introduction

This article describes the physical properties of less rapidly[1–9] and of rapidly quenched Heusler alloys with its frozen in compositional disorder and competing magnetic interactions. This is due to the excess Mn atoms interacting both ferromagnetically − because of the occupation of atomic sites in the original Mn sublattice − and antiferromagnetically because of the occupation of the excess Mn of atomic sites of the Z element in Ni–Mn–Z with Z = Al, Ga, In, Sn, Sb (see

Figure 1[10]). Experimental isofield magnetization curves for Ni–Mn–In alloys covering the first-order magnetostructural transition are shown in **Figure 2**[11–13]. For a recent review which highlights this magnetostructural transitIon, see Ref. [14]. Its impact on the so-called inverse magnetocaloric effect is highlighted in Ref. [15].

Figure 3 shows typical results of Monte Carlo simulations obtained for the magnetostructural transition for a series of Mi-Mn-In based alloys using the model defined in the Appendix showing large magnetocaloric effects (MCE).[15] Note that the magnetostructural transitions shown in Figure 3 correspond to those of very rapidly quenched samples, since the standard atomic relaxations during the *ab initio* calculations do not consider diffusion or similar relaxation processes.

If Co is added to the rapidly quenched Ni-Mn-In alloys, the magnetostructural transformation does not vanish, but the transformation becomes steeper because of the enhanced ferromagnetic component, compare **Figure 4**.

Prof. P. Entel, PD Dr. M. E. Gruner, Prof. M. Acet
Faculty of Physics and Center for Nanointegration, CENIDE, University Duisburg-Essen, 37048 Duisburg, Germany
E-mail: entel@thp.uni-duisburg.de

PD Dr. S. Fähler
IFW Dresden, P.O. Box 270116, 01171 Dresden, Germany

Dr. A. Çahır
Muğla Üniversitesi, Metalurji ve Malzeme Mühendisliği Bölümü, 4800 Muğla, Turkey

Prof. R. Arróyave, Dr. T. C. Duong, Dr. A. Talapatra
Department of Materials Science & Engineering, A&M University, College Station, Texas 77843, USA

Dr. S. Sahoo
Institute of Materials Science, University of Connecticut, CT 06269, USA

Dr. L. Sandratskii
Max Planck Institue of Microstructure Physics, Weinberg 2, 06120 Halle, Germany

Dr. S. Mankowsky
University of Munich, Department of Chemistry, Butenandstr. 5–13, 81377 Munich, Germany

Dr. T. Gottschall, Prof. O. Gutfleisch
Technical University Darmstadt, Institute of Materials Science, 64287 Darmstadt, Germany

P. Lázpita, V. A. Chernenko, J. M. Barandiaran
BCMaterials and Department of Electricity and Electronics, University of Basque, Basque, Spain

Dr. V. V. Sokolovskiy, Prof. V. D. Buchelnikov
Condensed Matter Physics Department, Chelyabinsk State University, 454021 Chelyabinsk, Russia

Dr. V. V. Sokolovskiy
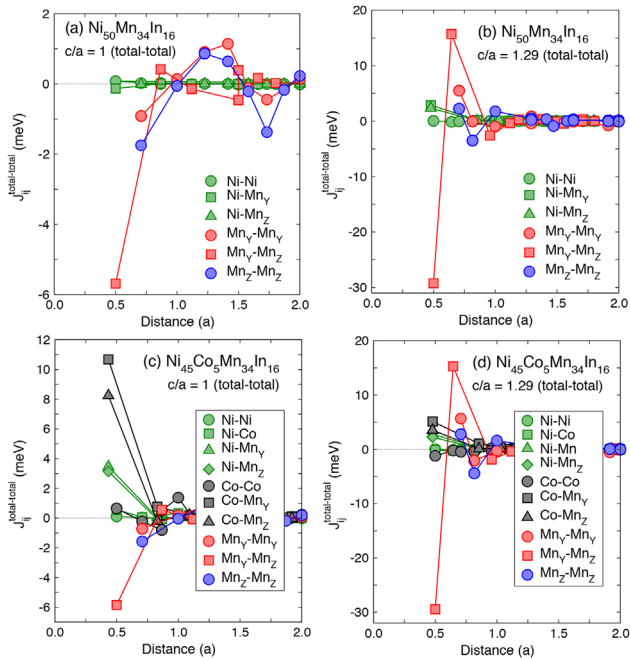National University of Science and Technology "MIS&S", 119049 Moscow, Russia

Figure 1. Magnetic exchange interactions of cubic $Ni_{50}Mn_{34}In_{16}$ for austenite (a) and martensite with a tetragonal distortion of $c/a = 1.29$ (b) and for the corresponding alloy containing 5% Co in (c) and (d). Plotted are the total of the interaction constants consisting of all $s-p$ and d electron contributions (total). For details see the corresponding decomposition of Mn-rich $Ni_{50}Mn_{30}Ga_{20}$ in Ref. [10]. The notation is obvious: The first atom is always at the origin and the distance between the atom sites is n units of the lattice constant. Positive exchange interactions are ferromagnetic and negative exchange interactions are antiferromagnetic ones.
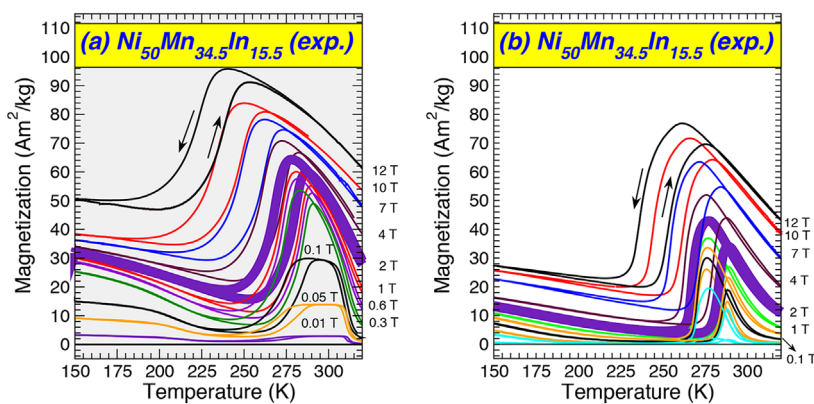

Figure 3. Results of Monte Carlo simulations for a series of Ni–Mn–In alloys. The magnetostructural transition shows hysteresis where the hysteresis width is in most cases of the same order although the jump $\Delta\mu(t)$ is different. The largest jump is shown when Co and Cr are added to Ni–Mn–In. This alloy also exhibits the largest MCE which is of the order of $\Delta T_{ad} \approx 10$ K.[15]

The magnetic nature has been recently studied for other Ni-Mn based metamagnetic systems, primarily for Co-added Ni-Mn-Z with Z = In, Sn, and Sb and various explanations of the magnetic behavior of martensite have been proposed: paramagnetism, antiferromagnetism, superparamagnetism, re-entrant spin-glass, superspin glass, etc.[14,16–18] Note that all spin-glass discussions automatically involve the possibility of strain-glass formation due to the coupling of the spins to the local strain fields arising from atomic disorder.

Superparamagnetic domains in a paramagnetic matrix have been shown to exist in the martensitic phase of $Ni4_{45}Mn_{36.5}In_{13.5}Co_5$ evolving to a superspin glass on cooling below a critical temperature[19] Superparamagnetic and superspin-glass behavior have been also observed in $Ni_{50-x}Co_xMn_{39}Sn_{11}$ ($0 \leq x \leq 10$), where the superparamagnetic state is formed by magnetic clusters distributed in a weak magnetic matrix, which has directly been confirmed by small-angle neutron scattering.[20] For completeness, we give reference to the work of Kainuma's and Chaddah's groups which performed experiments like those shown in Figure 4 some years before for Ni-Co-Mn-In alloys, see **Figure 5**.[21–26] As Figure 4, Figure 5 shows results of rapidly quenched samples.

Note that the shift of the isofield magnetization curves over a temperature interval covering the magnetostructural transition in Figures 4 and 5 has already been postulated by a 30-year old model calculation of structural and magnetic interactions in a two-fold degenerate band model of e_g symmetry using a model Hamiltonian for coexisting magnetic and martensitic phases[27,28] and a simple Hartree–Fock approximation. This leads for the rapidly quenched alloys to a typical shift of the martensitic transformation temperature to lower temperatures and finally to the arrest

Figure 2. Isofield magnetization curves of $Ni_{50}Mn_{34.5}In_{15.6}$ showing first-order magnetostructural transformation from weak magnetic martensite to ferromagnetic austenite. The $M(T)$ data from more ordered alloys (a) are very different from disordered alloys shown in (b). We think that this could be related to the order and its influence on the Curie temperature. For both cases, the shift of the martensitic transformation with applied field is clearly visible. Data provided by P. Lazpita Arizmendiarreta. With increasing magnetic field the jump is reduced in both cases and vanishes for very large fields (saturation magnetization) or the transformation can become kinetically arrested, when the driving force $\Delta G \approx \Delta S \times \Delta T$ becomes smaller and smaller. (a) Copyright AIP 2013,[11] (b) coyright IOP 2013.[12]

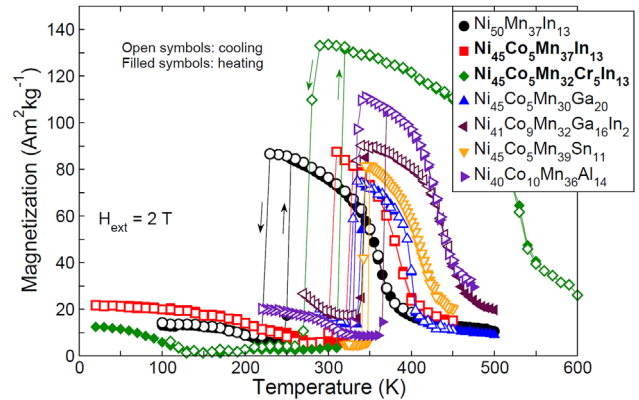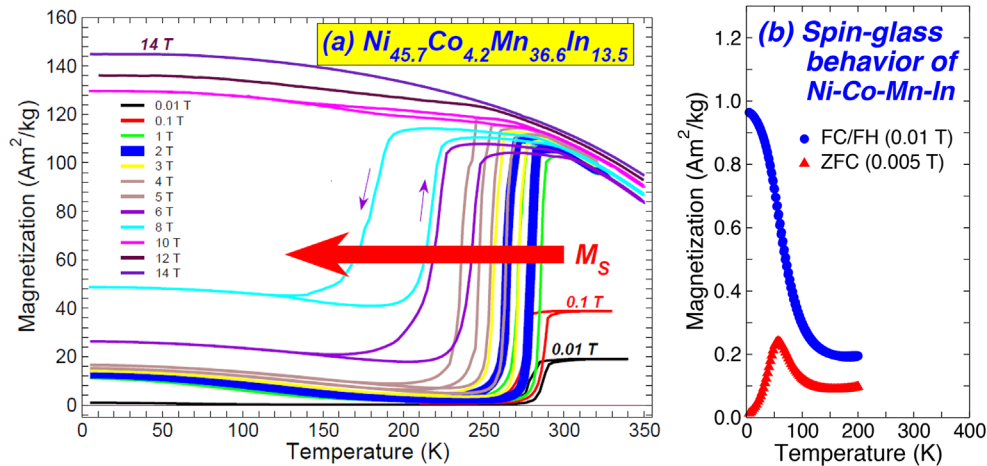**Figure 4.** (a) Shift of isofield $M(T)$ curves of Ni–Co–Mn–In with external magnetic field. For 14 T the magnetization curve is saturated.[30] Figure (b) shows that spin-glass behavior emerges if the measuring protocol of the magnetization is done according to field cooling and field heating.

of the martensitic transformation (kinetic arrest phenomenon[14,16–18]). Figure 5 shows the shift of the magnetization curves of $Ni_{45}Co_5Mn_{36.7}In_{12.3}$ with increasing magnetic field to lower temperatures.[21] We obtain for the shift of the martensitic transformation temperature [27,28],

$$\frac{\Delta T_{MS}}{T_{MS}^0} = -\left(\frac{\mu_B H}{k_B T_{MS}^0 (1 - U_{\text{eff}}\rho(\varepsilon_F))}\right)^2. \quad (1)$$

The Heusler alloys exhibit remarkable features like the magnetic shape-memory effect which has recently been highlighted by Planes et al.,[14] and first-order coupled magnetic and structural (magnetostructural) phase transitions. Figure 2 shows such transitions for (Co doped) Ni–Mn–In.[11,12,14] In contrast to the rapidly quenched alloys we describe also the physics of the less
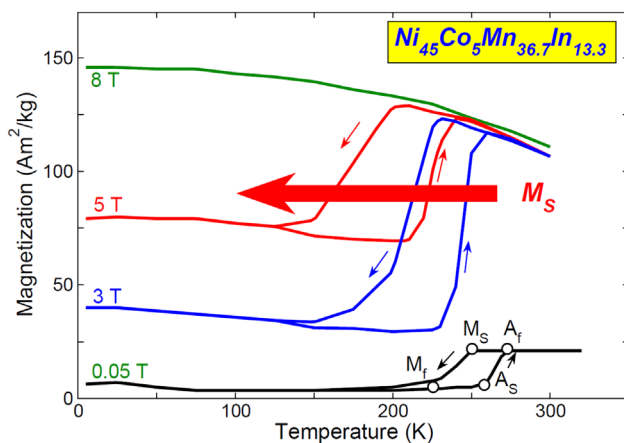
rapidly cooled alloys where the temper-annealed samples of $Ni_{50}Mn_{45}(Al, Ga, In, Sn)_5$ are not stable but decompose into ferromagnetic L2$_1$ Heusler part $Ni_2Mn(Al, Ga, In, Sn)$ and antiferromagnetic L1$_0$ NiMn. This type of segregation leads to new functional properties as the quenching under magnetic fields to ferromagnetic Heusler-type precipitates with a paramagnetic core give rise to vertically shifted magnetization loops.[5] Shell-ferromagnetism, noncollinear magnetism and skyrmions, which may lead to new exiting functional properties of Heusler alloys.[5,31–34]

2. Magnetostructural Phase Transition of Rapidly Quenched Heusler Alloys

Figure 2 shows the structural transformation between the high-temperature ferromagnetic austenite and the low-temperature weak magnetic, or antiferromagnetic (or paramagnetic) martensite as well as the shift of the martensitic transformation with applied magnetic field in $Ni_{50}Mn_{34.5}In_{15.5}$ (experimental data provided by P. Lazpita[11,12]).

Note that the isofield magnetizations curves of Figure 2 are not the result of a very fast quenching of the alloy, but some partial order prevails although the degree of order retained has never been specified in detail.[12] Another set of isofield curves for rapidly quenched alloys is shown in **Figure 6** for $Ni_{41}Co_9Mn_{32}Ga_{16}In_2$.[13] It also shows the superelasticity of the Heusler alloys.

The occurrence of the isothermally magnetic-field induced transformation at different temperatures is evident and allows to discuss magnetization and entropy changes, ΔM and ΔS, as a function of the applied field as predicted by the Clausius-Clapeyron equation $dT/dH = \mu_0 \Delta M/\Delta S$. The martensitic transformation is accompanied by a drastic drop in magnetization, favoring the magnetic field-induced reverse transformation, demonstrating the metamagnetic behavior.

Note that in disordered $Ni_{50}Mn_{34.5}In_{15.5}$ alloy (rapid quenching) the jump-like curve of of ΔM across the martensitic

Figure 5. Isofield magnetization curves of $Ni_{45}Co_5Mn_{36.7}In_{13.3}$ across the first-order magnetostructural transformation in fields of 0.05, 3, 5, and 8 T showing the shift of martensitic transformation with applied field to lower temperatures. From the fields H_{Af}, H_M, and $H_0 = (H_{Af} + H_M)/2$ the magnetic field-temperature phase diagram can be evaluated showing the kinetic arrest phenomenon, see also Ref.[29] Figure adapted from Ito et al., copyright AIP (2008).[21]

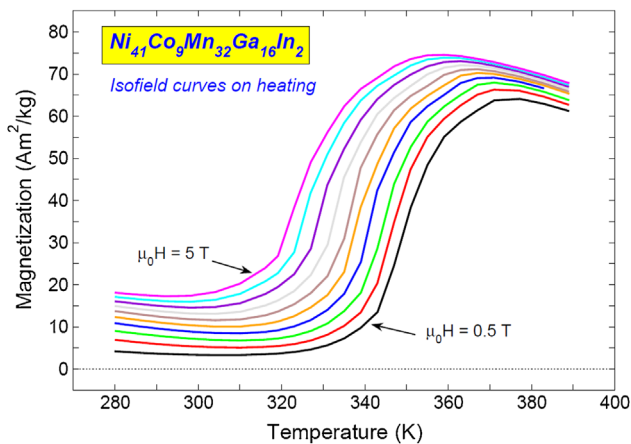**Figure 6.** Isofield magnetization curves $M(T)$ on heating of the martensitic transformation of $Ni_{41}Co_9Mn_{32}Ga_{16}In_2$ for $0.5 < \mu_0 H < 5$ T with field step of $\mu_0 H = 0.5$ T (data provided by G. Porcari[13]).

Figure 7. Structure of stoichiometric Ni_2MnGa (X_2YZ). The arrows indicate the exchange of Mn with either Ga or Ni. In both cases *ab initio* calculation of the magnetic coupling constants reveals antiferromagnetic interactions between the spins of Mn on the original sublattice (Mn_Y) and on the Z-sublattice (Mn_Z) or on the X-sublattice (Mn_X).

transition is steeper and increases with field while it remains nearly constant for the more ordered sample (slower cooling).[12]

Hence, the change of slope of $dT_M/\mu_0 dH = \Delta M/\Delta S$ may be related to the decrease of ΔS with applied field. However, for both, more ordered and more disordered alloys, the entropy change amounts to $\Delta S \approx 5$ J/(kg K), which originates mostly from the lattice contribution being larger than the magnetic entropy change across the magnetostructural transformation.

With respect to the theoretical modeling of magnetostructural transition, we have adopted a combined effort consisting of *ab initio* modeling of the complex scenario of magnetic exchange interactions in Ni-Co-Mn-In combined with Monte Carlo simulations of an effective spin model (Potts model for the multi-spin interactions in Heusler alloys), where the exchange integrals serve as input. The Hamiltonian used to calculate the magnetocaloric properties consists of the Potts model with coupling to the structural (elastic) components which allows to simulate magnetoelastic interactions and martensitic transformations (see Appendix).

The prototype magnetic Heusler system Ni_2MnGa consists of four interpenetrating fcc lattices (see **Figure 7**) with a phase transition to a tetragonal structure upon cooling below 212 K[35] and a magnetic transition to ferromagnetic order (where experimental and calculated Curie temperatures, using *ab initio* exchange coupling constants, are close to each other, $T_C \approx 376$ K[35,36]). The most recent phase diagram with some new data of intermartensitic transition is shown in **Figure 8**.[37] Phonon softening in Heuslers underlines the influence of Fermi surface nesting to explain the origin of martensitic instabilities.[38] With respect to shape memory properties, the reorientation of the tetragonal unit cell can be induced either by a magnetic field of by mechanical stress.[39–43] With onset of martensite, the Curie temperature rapidly drops to low values.

In this context it is important to note that the coexistence of austenite, adaptive 14M phase and tetragonal martensite in Ni-Mn-Ga and other Heusler alloys and the role of adaptive martensite of modulated shape memory alloys are beneficial for the formation of martensite and by this for shape memory properties because of elastic energy minimization.[44,45] It is also
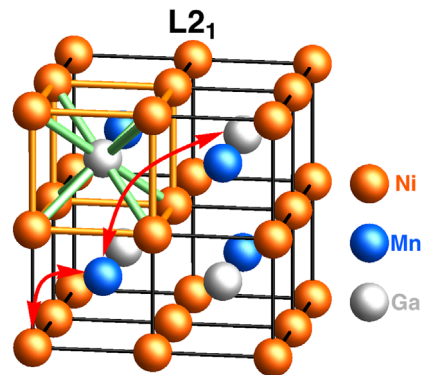
important to note that the modulated structure is not an equilibrium structure but a nanoscale microstructure of non-modulated martensite.

In addition to Heusler alloys exhibiting spin-glass features, we also find alloys with a completely new type of glassy behavior, which can arise from the disordered nature of displacement fields due to non-stoichiometric Heusler alloys or for a sufficient amount of impurities. This phenomenon has been called strain-glass, for example, see **Figure 9**.[46] We have a ferromagnetic strain-glass phase because the underlying intermetallic phase is ferromagnetic (FM austenite, FM martensite, and FM strain glass). The strain-glass phase arises because of the disorder induced frozen strain of the intermetallic alloy and the additional local strains arising from the Co impurities, which destroys the long-range strain features of martensite. This leads to a ferromagnetic strain glass with coexisting short range strain ordering and long range ordering of the magnetic moments, where Co essentially suppresses the long range strain ordering of martensite and enhances the ferromagnetic exchange.[46] An example for a strain-glass phase in Ni-Mn-Ga alloys with Co as impurity is shown in Figure 9. We find a ferromagnetic strain-glass phase because the underlying intermetallic phase is ferromagnetic (FM austenite, FM martensite, and FM strain glass). The strain-glass phase arises because of the disorder induced frozen strain of the intermetallic alloy and the additional local strains arising from the Co impurities, which destroys the long-range strain features of martensite. This leads to a ferromagnetic strain glass with coexisting short range strain ordering and long range ordering of the magnetic moments, where Co essentially suppresses the long range strain ordering of martensite and enhances the ferromagnetic exchange.[46]

For the quenched magnetic Heusler alloys Ni-Mn-Ga and Ni-Mn-Sn with Mn excess, Figure 8 shows the typical behavior in the temperature versus electron concentration plane with austenite (L2$_1$ structure) and martensite (L1$_0$ structure) and intermartensitic modulated structures. Besides spin-glass phases we also find strain-glass phases in most of the Mn excess region, where the strain-glass emerges because of local disorder beyond a certain threshold.
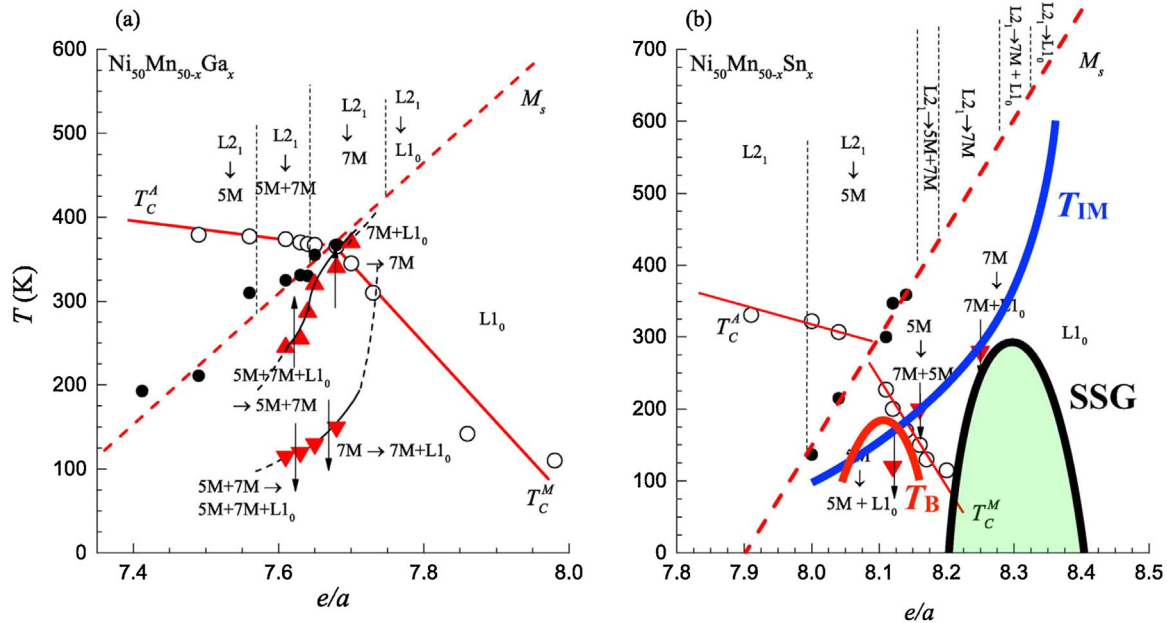
Figure 8. Phase diagrams of (a) $Ni_{50}Mn_{50-x}Ga_x$ and (b) $Ni_{50}Mn_{50-x}Sn_x$ with austenite–martensite transitions (filled circles) and intermartensitic transitions (triangles up and down). Open circles mark the Curie temperatures of austenite and martensite. T_{IM}, SSG and T_B mark the intermartensitic transition line, the super-spin-glass region and the blocking temperature, respecively. The phase diagram has been adapted from Çahir, copyright AIP (2015).[37]

We have investigated the magnetocaloric properties of Ni-Mn-(Ga, In, Sn) alloys by means of first-principles *ab initio* calculations and Monte Carlo simulations. These alloys show giant magnetocaloric effects, especially if a few per cent Co and Cr are added to the alloys.[15,47] The extra magnetic ions occupy regular sites of the Heusler lattice and can enhance the magnetization jump and adiabatic temperature change at the magnetocaloric transition.
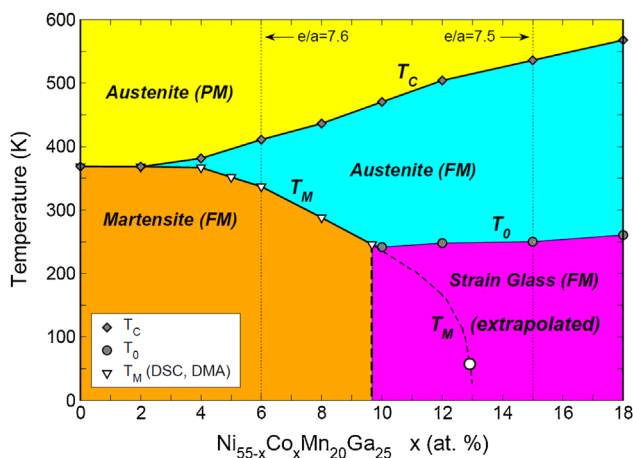

Figure 9. Phase diagram of $Ni_{55-x}Co_xMn_{20}Ga_{25}$ showing the paramagnetic and ferromagnetic austenite phases, ferromagnetic martensite as well as the ferromagnetic strain glass phase (calculation of the extrapolated T_M is also shown). Ferromagnetic martensite exists to rather high concentrations of Co impurities. The strain glass phase exists between 10% Co and more than 18% Co. Phase diagram adapted from Wang et al.[46]

On the other hand, we have systematically investigated the segregation tendencies which occur in these alloys near the martensitic transformation, see Refs. [3,4] and [5,7,8].

Other remarkable features like the magnetic shape-memory and magnetocaloric effects have recently been highlighted by Planes et al.[14] The isothermal entropy and and adiabatic temperature changes associated with the magnetostructural transition can be evaluated by Monte Carlo simulations using

$$\Delta S_{mag}(T, H) = \mu_0 \int_0^H dH' \left(\frac{\partial M}{\partial T} \right)_{H'}, \tag{2}$$

$$\Delta T_{ad}(T, H) = -T \frac{\Delta S_{mag}(T, H)}{C(T, H)}. \tag{3}$$

Figure 10 shows the magnetocaloric effect of the alloy $Ni_{45}Co_5Mn_{32}Cr_5In_{13}$ with an adiabatic temperature change of nearly 10 K.[15,48] This is a record value for Heusler alloys and is close to $\Delta T_{ad} = 12.9$ K of Fe–Rh[49,50] and 9.2 K for $Fe_{49}Rh_{51}$ on the first application of a magnetic field of $\Delta\mu_0 H = 1.9$ T which remains as high as 6.2 K during the cycling in alternated field of the same magnitude.[51] It has been shown that a magnetic state change of Rh between antiferromagnetitransm (with a Rh moment of $0\mu_B$) and ferromagnetism ($\sim 0.9\mu_B$), accompanied by a sgnificant change in electronic structue, is the main origin of the metamagnetic transiton.[52] To be more precise, it is the cooperative contribution of electronic, magnetic and vibrational degrees of freedom which is responsible for the giant magnetocaloric effect in FeRh.[53]
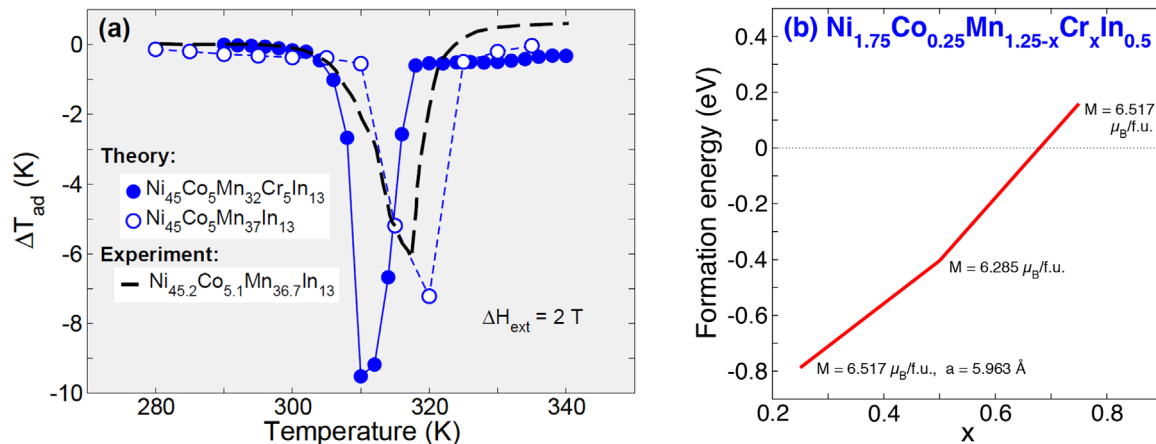
Figure 10. (a) Adiabatic temperature change of Ni–Mn–In alloys doped with Co (open circles) compared with experimental data (dashed line) and doped with Co and Cr (blue circles).[15] In the latter case the adiabatic temperature change approaches 10 K in an external field of 2 T which is close to the magnetocaloric effect shown by Fe–Rh. (b) Formation (mixing) energy of $Ni_7CoMn_5CrIn_2$ calculated as difference between the total energy of the 16-atom L2$_1$ supercell with ferromagnetic order and all partial total energies of the pure elements (with stability up to $x = 6$ at.% Cr).[48]

The alloy $Ni_{45}Co_5Mn_{32}Cr_5In_{13}$ is stable with respect to decomposition into all individual elements,

$$E_{mixing} = E_{Ni_7Co_1Mn_5Cr_1In_2} - \frac{7}{16}E_{Ni} - \frac{1}{16}E_{Co}$$
$$- \frac{5}{16}E_{Mn} - \frac{1}{16}E_{Cr} - \frac{2}{16}E_{In}. \quad (4)$$

However, the correct decompositiom corresponds more to a dual alloy formation, as will be explained below.

3. Noncollinear Magnetism

In this section we briefly discuss the possibility that we may have to address noncollinear spin configurations in rapidly and less rapidly quenched Heuslers when we discuss magnetic ordering in Heusler alloys. From the magnetic exchange interactions shown in Figure 1 for non-stoichiometric Ni–(Co)–Mn–In alloys we know that non-ferromagnetic spin arrangements can easily be achieved especially in case of tetragonal distortions of the cubic lattice, which explains the breakdown of ferromagnetic order for most of the martensitic phases of Ni–Mn–(Al, Ga, In, Sn)–Z with Z = Co or Cr. This behavior may also lead to noncollinear spin arrangements. We have tested this for a 16-atom supercell of $Ni_7Co_1Mn_6In_2$ and found indeed a noncollinear spin arrangement which is slightly lower in energy compared with ferromagnetic order,[54,55] see **Figure 11**.

The non-cubic environments for the non-stoichiometric alloys may help to enforce the tendencies for additional relaxation forces and tetragonal distortions and may thus help to stablize noncollinear spin configuations. Thus we speculate that non-stoichiometry and addtional local atomic relaxations due to impurities in the alloys may also lead to cluster spin glass phases[20] and new glassy states like strain glass phases.[56]

We would like to emphasize that strain glasses seem to be by now well established phases since this new glassy feature has been observed for many intermetallic systems. Besides the magnetic Heusler alloy Ni–Co–Mn–Ga cited above,[46] there are other intermetallics which show strain glass characteristics, for a recent review, see Ref. [56].

With respect to the non-cubic enviroment of atoms we note that relaxation of atoms may depend on the crystallographic direction, so that a plot of the "crystallographic average" of the relaxed state of atoms may become meaningful. If we do that for the magnetic configurations of "ferromagnetic" (all spins parallel) and "ferrimagnetic" (allowing spin reversal for the spins of Mn) solutions, we may plot for each of these states $E_{average} = 1/3E_{c\|z} + 2/3E_{c\|x}$. This leads for $Ni_7Co_1Mn_6In_2$ to the result shown in **Figure 12**.

Here, we have assumed that the ferromagnetic solution is a high-spin (HS) state and the ferrimagnetic solution for martensite is a low-spin (LS) state which can be smoothly joined by a noncollinear solution as in Fe–Ni Invar.[57] This further stresses the importance of noncollinear spin configurations for Heusler alloys, which exhibit the inverse magnetocaloric effect.

With a different numerical tool, the so-called fixed spin moment method, we have calculated the many multiple local energy minima, which occur between the HS state of austenite
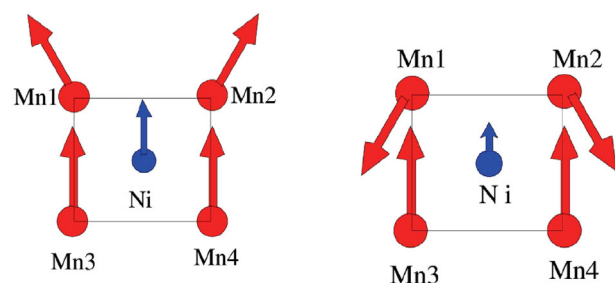

Figure 11. Noncollinear magnetic moments between neighboring Mn atoms in a 16-atom supercell for $Ni_7Co_1Mn_6In_2$. Spin configurations of the left and right pictures have nearly equal energy and have been calculated by Refs. [54] and [55], respectively.
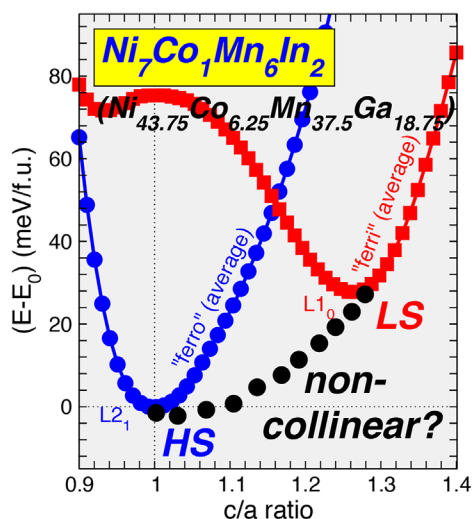
Figure 12. Energy landscape of austenite and martensite formation for $Ni_7Co_1Mn_6In_2$ (16-atom supercell, which corresponds to $Ni_{43.75}Co_{6.25}Mn_{27.5}In_{18.75}$). Because of non-stoichiometry, the symmetry is not cubic, hence the tetragonal distortion in x an z direction yield different results. Plotted are average values $E_{average} = 1/3E_{c\|z} + 2/3E_{c\|x}$ for ferromagnetic and ferrimagnetic (spins of Mn on In sites reversed) solutions, respectively. We assume that high spin (HS) and low spin (LS) states can be joined smoothly as in Invar[57] as indicated by the back dots.

and LS state of martensite, allowing to bridge the gap between these states.[58] This also speaks in favor of the existence of noncollinar magnetic spin configurations in magnetic Heusler alloys and may be the origin of complex hysteresis behavior, see **Figure 13**.[59]

Indeed, the chemical disorder of the Heusler alloys, the resulting spin configurations of austenite and the weak magnetism of martensite will also influence the hysteresis behavior of the alloys around the magnetostructural phase transition. Figure 13 shows the formation of minor hysteresis loops in the magnetization curve around the martensitic
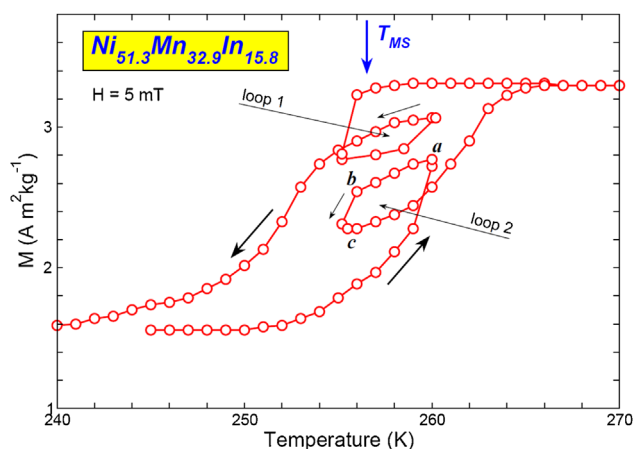
transformation temperature T_{MS}. Before measurement, a sample of $Ni_{51.3}Mn_{32.9}In_{15.8}$ was brought to a temperature below T_{Mf} where it is in the pure martensitic state. Figure 12 shows the case when the sample is warmed to about 260 K corresponding to a state on the reverse transformation branch of the thermal hysteresis (point a). At this point, the sample has partially transformed into the austenitic state. The ratio of the amount of austenite-to-martensite is characterized by the parameter $r = [M(T) - M(T_{Mf})]/[M(T_{MS}) - M(T_{Mf})]$ where $M(T)$ is the magnetization value within the temperature range of the hysteresis. When the temperature is now gradually reduced, r remains initially unchanged, so that the change in $M(T)$ is initially weak (path $a \rightarrow b$). But, when the temperature approaches and begins to fall below T_{MS}, martensite begins to rebuild and $M(T)$ decreases (path $b \rightarrow c$). If the temperature of the sample is increased from point c, r changes in favor of austenite, and $M(T)$ eventually returns to the s.

At each step, the complex spin configurations will determine $M(T)$. Repeating the process will cause the state of the system to remain on a minor loop (loop 1), whereby r will be reversible in the path of this minor loop. A similar minor loop (loop 2) can be found for the case when the sample is brought to a state on the forward transformation branch from temperatures well within the austenite state.

4. Dependence on the Cooling Rate after Heat Treatment

In this section we briefly discuss the magnetization jump of Ni-Mn-In alloys as a function of the heat treatment which yields different degrees of order in the alloys. The influence of annealing on the magnetization curves is shown in **Figure 14** [60]).

For high annealing temperature A_Q, for example, $A_Q = 1173$ K and rapid quenching of $Ni_{50.2}Mn_{33.4}In_{16.4}$, the form of the magnetization curve is very steep, but with

Figure 13. Minor hysteresis loops within the thermal hysteresis of the magnetization under 5 mT for $Ni_{51.3}Mn_{32.9}In_{15.8}$, a non-stoichiometric Ni–Mn–In alloy.[59]

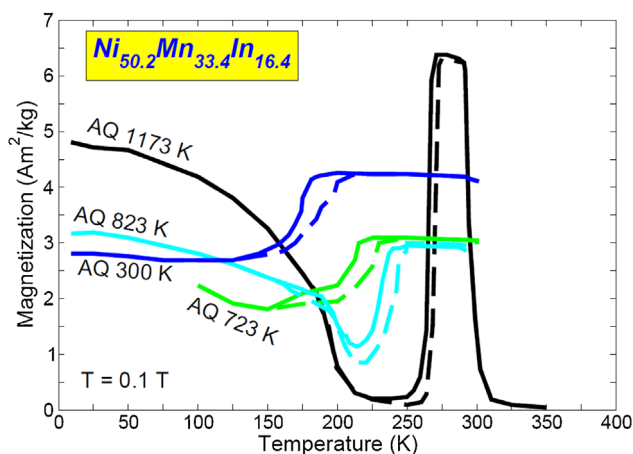**Figure 14.** Temperature dependence of magnetization in a field of 0.1 T of $Ni_{50.2}Mn_{33.4}In_{16.4}$ subject to four different heat treatments labeled AQ 1173 to AQ 300 K, which yield different degrees of order. The slowly cooled sample labeled AQ 300 K exhibits the largest degree of order. Figure taken from Ref. [60], copyright Elsevier (2012).

decreasing annealing temperature the forward and reverse martensite transformation temperatures are smoothed, for example, in very low field of 10 mT.[60] In order to retain states with different degrees of LRO (long-range order), the alloys were subjected to a 30 min annealing treatment at three different temperatures followed by quenching into ice water. Another piece of the same alloy was slowly cooled from 1173 K (labeled AQ 300 K) for comparison with the the quenched samples.

Similar magnetization curves for ordered and less ordered $Ni_{50} Mn_{34.5}In_{15.5}$ alloys were obtained by Barandiaran et al. in Refs. [11,12]. Rectangular-like magnetization curves have also been observed for $Ni_{50}Mn_{35}Sn_{15}$ alloys together with a splitting of ZFC (zero-field cooled), FC (field cooled), and FH (field heated) curves.[61] As already mentioned, in a series of publications a systematic adjustment of composition which fixes the magnetic ordering and giant magnetocaloric effect was discussed.[3,4] It appears that for the Ni-Mn-Sn alloy system, this compositional tuning has dramatic effects on the microstructural development. It was concluded that the martensitic transformation occurs only for those compositions where the single phase $L2_1$ has been retained in a metastable state on cooling.[3] The off-stoichiometric Ni–Mn–Sn Heusler alloys, which undergo a martensitic transformation, are metastable in a temperature range around $T = 773$ K.

There are other experiments in which the thermal stability, for example, of Ni–Mn–Ga alloys in the temperature range 620–770 K was investigated.[62] If the ratio e/a is increased by substitution of Ga by Mn, very stable alloys are achieved. Other interesting aspects like large precipitates, "self-patterning", influence of vacancies on modulated and non-modulated phases were investigated.[63–65] This short list of discussing properties of non-stoichiometric Heusler alloys is by far not complete, but, it gives an impression on the rich properties of functional magnetic Heusler alloys. We remind the reader of the shift of the martensitic transformation temperature for the rapidly quenched alloys which is proportional to the square of the external magnetic field and which was already predicted by Ghatak et al.[27,28] The associated so-called kinetic arrest phenomenon still requires further simulations.

5. On the Nature of Decomposition in Heusler Alloys

The structural metastability of $Ni_{50}Mn_{45}Ga_5$ alloys is an inherent property of the $Ni_{50} Mn_{50-x}X_x$ alloys with X as Ga, In and Sn.[3–5,7,8] The alloys transform during temper-annealing to a dual-phase composite alloy, cubic $L2_1$ Heusler and $L1_0 Ni_{50}Mn_{50}$. This may lead to time-dependent effects as, for example, supercells with non-stoichiometric composition show strong atomic relaxations because of non-cubic environment of the individual atoms. This directly probes the effect of disorder and may cause the onset of segregation for alloys close to martensitic transformation (this may also trigger the $L2_1$−B2 transformation of Ni–Mn–In,[1] Ni–Mn–Al,[66] and Ni–Mn–Ga[67]).

The decomposition into a dual-phase composite alloy is a very peculiar type of decomposition but appears to be lowest in energy. Results for the mixing energies of Ni–Mn–In and Ni–Mn–Sn alloys are shown in **Figure 15**. This is different from the B2–$L2_1$ transition (compare **Table 1**).
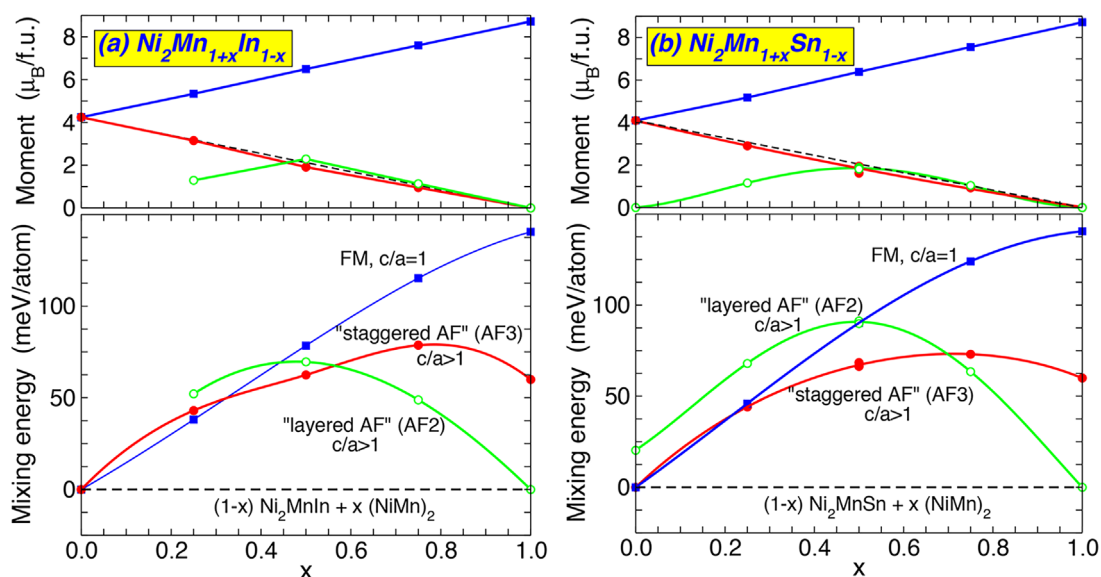

Figure 15. Mixing energies and magnetic moments of (a) $Ni_2Mn_{1+x}In_{1-x}$ and (b) $Ni_2Mn_{1+x}Sn_{1-x}$ for two different antiferromagnetic spin orderings, AF2 and AF3, which are illustrated in **Figure 16**. The mixing energy is calculated by assuming that over the whole concentration range the decomposition of the alloy will lead to a dual-phase composite alloy causing $L2_1 Ni_{50}Mn_{25}In_{25}$ and $L1_0 Ni_{50}Mn_{50}$. The Heusler precipitates are ferromagnetic while the antiferromagnetic matrix is assumed to have AF2 or AF3 ordering. (Here, AF2 refers to antiferromagnetically ordered layers which are coupled ferromagnetically, and AF3 referes to antiferromagnetic layers coupled antiferromagnetically.) The structures of antiferromagnetic Ni_8Mn_8 show considerable tetragonal deformations: "staggered AF" ($a = 5.076, c/a = 1.42$), "layered AF" ($a = 5.1066, c/a = 1.401$), see also **Figure 17**.
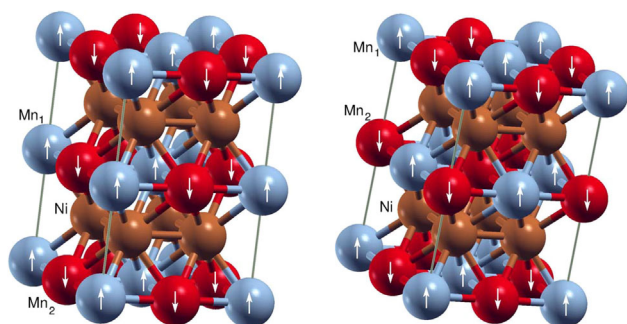
Figure 16. Antiferromagnetic spin structures, for which the mixing energies have been evaluated. Left: "layered AF" (AF2) and right: "staggered AF" (AF3) ordering.
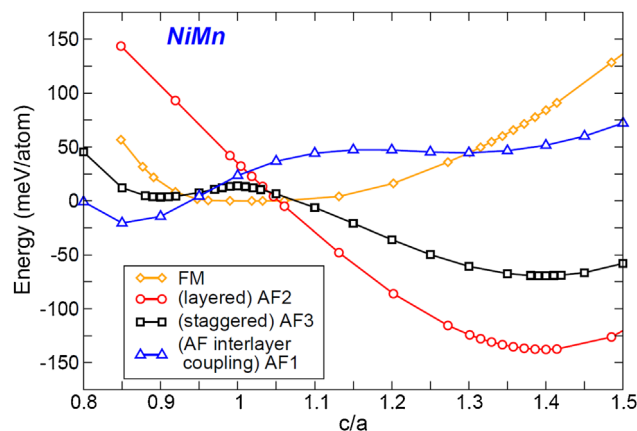

Figure 17. Total energy as a function of the tetragonal distortion c/a for different spin configurations of binary NiMn. The orange curve denoted as FM corresponds to a ferromagnetic alignment of the Mn spins whereas the other curves are associated with different antiferromagnetic alignments of the Mn spins. The red curve denoted as AF2 shows the ground state, which has been reported by Kasper and Kouvel.[69]

6. Ordering/Disordering, Segregation and Martensite Tranformation

The final phase diagram is shown in **Figure 18**. It is obvious that martensitic instabilities and segregation are close to each other in composition and are interrelated.

In order to explain the physical behavior of the influence of annealing and phase decomposition on the magneto-structural transitions in $Ni_{50}Mn_{39}Sn_{11}$ (blue star in Figure 18), we refer to the work of Ref. [3] regarding the heat treatment of the alloys. To study the role of chemical ordering in fine-tuning their magnetostructural properties, the alloys were first annealed for 4 weeks at 1223 K to achieve structural and compositional homogeneity, and were then further annealed for 1 week ($\sim$150 K below the reported B2 to $L2_1$ transition at 773 K) to increase the degree of chemical ordering. For 11 at. % Sn, this anneal resulted in a dramatic change in the magnetic ordering temperature. Following the 1223 K anneal, the sample exhibited ferromagnetic ordering at 140 K. After the 773 K anneal, the ferromagnetic transition is at 350 K, a characteristic of the ferromagnetic austenite phase for alloys with $15 < x < 25$ content of Sn. The authors further find from transmission electron microscopy examination that the alloy decomposed into two phases with $x = 20$ and 1. From this result one can conclude that the martensitc transformation occurs only in those compositions where the single phase $L2_1$ has been retained in a metastable state on cooling.

Thus the driving force for the decomposition seems not to be directly related to the disordering–ordering B2/$L2_1$ phase

transition, which is at higher temperatures, it occurs for compositions near the martensitic instability. Nonetheless, in the spirit of a unified theory of disorder–order and martensitic transformations we expect the disorder–order and martensitic phase transition lines to cross, which would place the systems which segregate right into the interesting region of structural and disorder–order transformation. Experimentally it seems difficult to get information of disorder–order transformation at lower temperatures.

Our *ab initio* calculations of phonons for the disordered alloys confirm the existence of the martensitic instability near this critical concentration. Earlier calculations of Fermi surface nesting confirmed that nesting behavior is still present for the non-stoichiometric, disordered systems. The number of valence electron which is larger in Ni–Mn–Sn ($e/a \approx 8.2$) compared to stoichiometric Ni_2 MnGa ($e/a = 7.5$) just blows the Fermi surface up but does not lead to compete vanishing of nesting behavior.

There is a series of recent temper-annealing experiments on Ni–Mn–In,[5,8] Ni–Mn–Al,[6] Ni–Mn–Ga,[7] and Ni–Mn–Sn (to be published) alloy systems, all with high e/a ratios and very well separated in temperature from the B2/$L2_1$ disordering–ordering transition but also close to the martensitic transformation, which are as well marked in Figure 18, with post-annealing temperatures from 650 to 750 K, and which show similar effects of segregation than just explained for the Sn-sample. Indeed in the experimental setup one let the samples undergo the martensitic transformation to the $L1_0$ structure and subsequently observes the decomposition or segregation into a dual-phase composite alloy, where the two phases are identified to be cubic $L2_1$ $Ni_{50}Mn_{25}In_{25}$ and $L1_0$ $Ni_{50}Mn_{50}$.[5]

The results of decomposition for the Ni–Mn–In and Ni–Mn–Sn alloys have been calculated by assuming that the segregation follows the prescription in Figure 18:

Table 1. Energy difference between B2 and $L2_1$ structures calculated with VASP[68] for a fully relaxed 432-atoms supercell and $4 \times 4 \times 4$ k-points). Atomic positions and volume are fully relaxed. The distribution of atoms has been generated by a random number generator.

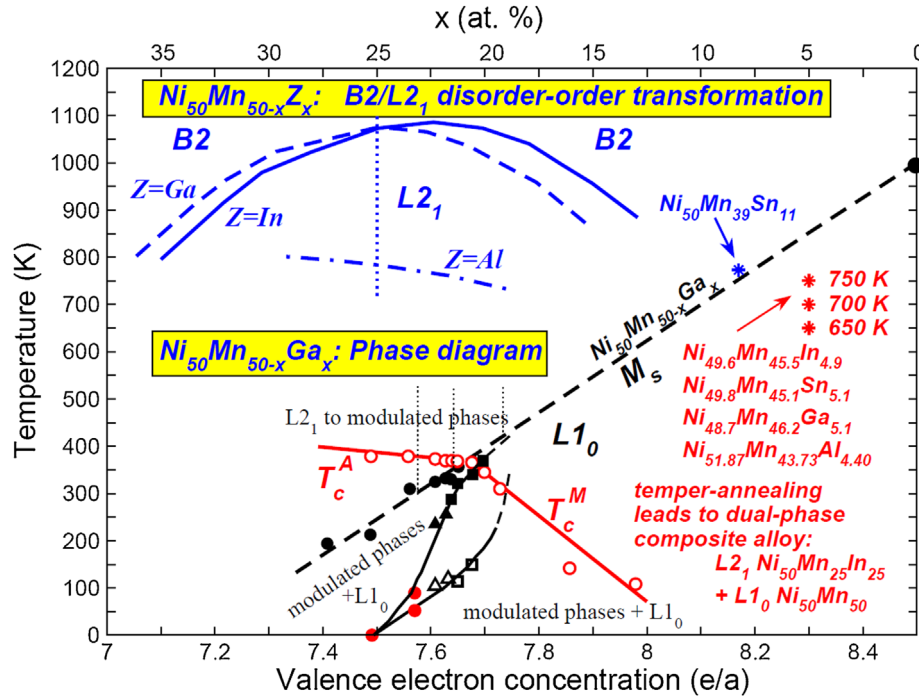| System	$\Delta E = E_{B2} - E_{L21}$
Ni_2MnAl	163 meV/f.u. = 41 meV atom^{-1}
Ni_2MnGa	198 meV/f.u. = 50 meV atom^{-1}
Ni_2MnIn	125 meV/f.u. = 32 meV atom^{-1}
Ni_2MnSn	359 meV/f.u. = 90 meV atom^{-1}

Figure 18. $B2/L2_1$ disorder-order tranformation of $Ni_{50}Mn_{50-x}Z_x$ as a function of x (upper axis) and e/a (lower axis) for $Z = Al$, Ga, In.[1] The crosses mark the alloy systems for which segregation has been investigated.[5,7,8] They are all very close to the martensitic transformation. The phase diagram of $Ni_{50}Mn_{50-x}Ga_x$ showing the austenite-martensite phases as well as its Curie temperatures which have been added to the plot.

$$E_{mixing} = E_{Ni_2Mn_{1+x}In_{1-x}} - (1 - x)E_{Ni_2MnIn} - xE_{(NiMn)_2}, \quad (5)$$

where the reference energy is the energy of the alloy decomposed into stoichiometric Ni_2MnIn and binary NiMn. We assume different antiferromagnetic configurations, layered (AF2) and staggered (AF3). The absolute values of the energies of segregation are quite large and approximately correspond to the temperature scale in Figure 18 of the decomposed alloys Ni–Mn–(Al, Ga, In, Sn).

It seems to be obvious that the decomposition into stoichiometric precipitates in NiMn antiferromagnetic background of all alloy systems listed in Figure 18 is energetically favored. The decomposed Heusler alloys all have high e/a rations near 8.3 which is in the martensitic region or very close to it. But segregation also occurs 150 K below the disorder-order transformation. So, it may be debated whether coexistence of disorder-order and martensitic tendencies may play a role in these alloys and have to be considered within the frame of a unified description for order-disorder and structural instability.

7. Concluding Remarks

The final phase diagram showing martensite and Curie temperatures of Ni–Mn–Ga, $B2/L2_1$ ordering temperatures measured so far as well as position of alloys undergoing decomposition in Figure 18 illustrates that the various instabilities must be very close to each other in energy and

are interrelated. More information will require additional first-principles calculations.

Appendix A

Calculational Details

The model Hamiltonian consists of a generalized q-states Potts model which includes structural degrees of freedom (for details see Refs. [15,70–72]):

$$\mathcal{H} = \mathcal{H}_m + \mathcal{H}_{el} + \mathcal{H}_{int}, \quad (6)$$

$$\mathcal{H}_m = -\sum_{\langle ij \rangle} J_{i,j}^m \delta_{S_i,S_j} - g\mu_B H_{ext} \sum_i M_i \delta_{S_i,S_g}$$
$$- K_{ani} \sum_i M_i^2 \delta_{S_i,S_{g'}}. \quad (7)$$

The $J_{i,j}$ are the magnetic exchange parameters for each Heusler system obtained from *ab initio* calculations. Since mapping of *ab initio* energies is only onto J_{ij} with unit length of spins, anisotropy field term and external field term must include explicitly the values of magnetic moments M_i, and M_i^2, where M_i is the *ab initio* value of magnetization of atom at site i (taken to be dimensionless), S_g is a ghost spin.[70] The Kronecker symbol restricts the spin–spin interactions to those between the same Potts-q states defined at lattice site $i = 1 \ldots N$. The spin moment of Mn is $S = \frac{5}{2}$ and we identify the $2S + 1$ spin projections with $q_{Mn} = 1 \ldots 6$. Likewise, we assume $S = 1$ for Ni with three Potts

states variables, and $S = \frac{3}{2}$ with four Potts states variables for Co. The Mn–Ni interaction is then simulated by letting the three q_{Ni} states interact with the first three q_{Mn} states.

Since the exchange parameters depend on the distance between the atoms, but, also on temperature and magnetic field, we may use a Taylor series expansion of the $J_{i,j}$ to obtain a further intrinsic dependence of the spin-spin interactions on elastic properties but also a dependence on the control variables temperature and magnetic field. This is left for future calculations.

The elastic and interaction terms, H_{el} and H_{int}, are defined by

$$\mathscr{H}_{el} = -\left(J + U_1 g\mu_B H_{ext}\sum_i \delta_{\sigma_i\sigma_g}\right)\sum_{\langle ij\rangle}\sigma_i\sigma_j$$
$$-K\sum_{\langle ij\rangle}\left(1-\sigma_i^2\right)\left(1-\sigma_j^2\right) \qquad (8)$$
$$-k_B T \ln p \sum_i \left(1-\sigma_i^2\right),$$

$$\mathscr{H}_{int} = 2\sum_{\langle ij\rangle} U_{i,j} M_i M_j \delta_{S_i,S_j}\left\{\left(\frac{1}{2}-\sigma_i^2\right)\left(\frac{1}{2}-\sigma_j^2\right)-\frac{1}{4}\right\}. \qquad (9)$$

Here, J and K are the elastic and $U_{i,j}$ and U_1 the magnetoelastic interaction constants, T is the temperature, and p the degeneracy of martensite, that is the number of possible martensitic variants. $\sigma_i = 1, 0, -1$ represents the deformation state at each site of the lattice ($\sigma_i = 0$ corresponds to the undistorted state whereas $\sigma_i = \pm1$ represents distorted states), σ_g is a ghost deformation state, whose value is that of the structural variant in an external magnetic field. Summation is done over all nearest neighbor pairs, for the spin-spin interaction we allow for more than nearest neighbor interactions. Furthermore we set $U_{i,j} = U$. To summarize, the extended Potts model in Eq. (6) allows us to describe magnetic, structural as well as coupled magnetostructural phase transitions. In order to calculate the average energy for a given temperature, we will use the same algorithm as discussed in Ref. [70].

The magnetization of the extended Potts model is obtained from

$$m_a = \frac{1}{N_a}\left(\frac{q_a N_{max}^a - N_a}{q_a - 1}\right) \qquad (10)$$

where atom a refers to Ni, $Mn_{Y,Z}$ and to Co_X, N_a is the number of atoms, N_{max}^a is the maximal number of identical magnetic atoms on the lattice and q_a denotes the number of magnetic states of each atom (the magnetic moments μ_a are taken from ab initio calculations). In order to take into account high-temperature austenite and low temperature martensite, we consider the volume fraction $f^{A(M)}$ of each phase for an estimation of the total magnetization. Hence,

$$M = M^A f^A + M^M f^M, \qquad (11)$$

$$M^{A(M)} = 2\left(1-\frac{1}{2}x\right)\mu_{Ni_X}^{A(M)} m_{Ni_X} + \mu_{Mn_Y}^{A(M)} m_{Mn_Y}$$
$$+\gamma\mu_{Mn_Z}^{A(M)} m_{Mn_Z} + x\mu_{Co_X}^{A(M)} m_{Co_X}, \qquad (12)$$

$$f^A = \frac{1}{N}\sum_i \sigma_i^{(0)}, \qquad (13)$$

$$f^M = \frac{1}{N}\sum_i \left(\sigma_i^{(-1)} + \sigma_i^{(+1)}\right) \qquad (14)$$

where x is the concentration of Co going onto the Ni sites and y is the concentration of Mn-excess going onto the Z-sublattice.

The extended Potts model may be used to calculate martensite and austenite phases as well as magnetic cluster-spin glass and strain-glass phases. The specific magnetic phase having lowest free energy for given composition (defect concentration), temperature and external magnetic field depends (dominantly) on the ab initio magnetic exchange parameters. Because of the magnetoelastic coupling, super-magnetoelastic behavior, magnetic cluster-spin glasses and strain glasses mutually interact.

Magnetic multi-domain states can be simulated by dvideeing the simulation cell into samller cells and fixing different q states to the individual cells (this mimics a polycrystalline alloy with respect to its magnetic properties). Values of magnetic anisotropy constants are estimated from ab initio calculations or from experimental values where available.

Using the strain variables σ_i, the strain order parameter (so-called Blume-Emery-Griffiths, BEG, model[73,74]) may be defined as

$$\varepsilon = \frac{1}{N}\sum_1^N \sigma_i. \qquad (15)$$

The order parameter ϵ is a measure of tetragonal distortion of the cubic phase. For $\varepsilon = 0$ the system is in the high-temperature cubic state whereas $\varepsilon = 1$ corresponds to the tetragonally distorted low-temperature phase.

Regarding hysteresis effects, we model first-order martensitic phase transitions with thermal hysteresis for sufficiently large biquadratic elastic interaction ($0.2 < K/J < 0.37$, for Ni-(Co)-Mn-In alloys we have adopted 0.23). Because of the magnetoelastic coupling the jump of the $M(T)$ curves is coupled to the martensitic transformation and exhibits hysteresis as well.

Figure 3 shows the large jumps $\Delta M(T)$ of Ni-Mn-In alloys (including $Ni_{45}Co_5Mn_{37}In_{13}$) across the magnetostructural transition obained from Monte Carlo simulations. The results agree qualitatively with experiment.[11,75] and point toward cluster-spin glass behavior with a freezing temperature of ca. 150 K in martensite.

The Hamiltonian can also be used to simulate the magnetocaloric proprties such as magnetic specific heat, isothermal magnetic entropy and adiabatic temperature changes across the magnetocaloric properties, following

ADVANCED
SCIENCE NEWS
www.advancedsciencenews.com

physica
status
solidi
pss b
www.pss-b.com

$$C_{\text{mag}}(T, H_{\text{ext}}) = \frac{1}{k_B T^2}\left[\langle \mathscr{H}^2\rangle - \langle \mathscr{H}\rangle^2\right], \qquad (16)$$

$$S(T, H_{\text{ext}}) = \int_0^T dT' \frac{C(T', H_{\text{ext}})}{T'}, \qquad (17)$$

$$\Delta S_{\text{mag}}(T, H_{\text{ext}}) = S(T, H_{\text{ext}}) - S(T, 0), \qquad (18)$$

$$\Delta T_{\text{ad}}(T, H_{\text{ext}}) = T(S, H_{\text{ext}}) - T(S, 0). \qquad (19)$$

For the total specific heat we add the lattice contribution using the Debye model.

So far, Monte Carlo results of isofield curves for $Ni_{50-x}Co_x Mn_{37}In_{13}$ and $Ni_{50-x}Co_x Mn_{39}Sn_{11}$ show indication of a cluster-spin glass phase, although FC/ZFC curves are difficult to obtain properly from the simulations. We have not yet attempted to simulate strain glass phases.

Appendix B

A Few Numerical Details

Regarding the *ab initio* calculations of mixing energies in Figure 15, we have perfomed the mixing enegy calculations of $Ni_2 Mn_{1+x}In_{1-x}$ and $Ni_2Mn_{1+x}n_{1-x}$ with respect to decomposition into $(1-x)Ni_2Mn(In, Sn) + x(NiMn)_2$ for all x using the VASP code[68] (generalized gradient approximation for the exchange correlation functional in the formulation of Perdew, Burke and Enzerhof (PBE).[76] With respect to the magnetic exchange interactions shown in Figure 1, we have performed SPR-KKR calculations for the effective exchange interactions J_{ij} using the KKR CPA method[77] where, following the prescription of Ref. [78], we obtain the J_{ij} from

$$J_{ij} = \frac{1}{4\pi} \int_{-\infty}^{\varepsilon_F} dE\left[\text{ImTr}\Delta_i\tau_\uparrow^{ij}\Delta_j\tau_\downarrow^{ji}\right], \qquad (20)$$

where Δ_i is the difference in the inverse single-site scattering t matrices for spin-up and spin-down states, $\Delta_i t_{i\uparrow}^{-1} - t_{j\downarrow}^{-1}$, and τ is the scattering path operator and the trace is over the product of the corresponding matrices. Further decomposition of the J_{ij} into interaction constants involving all $s-p$ and d elctrons is possible, see Ref. [10], which allows to discuss metamagnetic beahavior which seems to be associated with the partial compensation of ferromagnetic exchange interactions among the Ni–Mn_Y (Mn on the Mn sublattice) involving the t_{2g} electrons and the antiferromagnetic exchange interacions among the Ni–Mn_Y atoms involving the e_g electrons.

Moreover, the magnetostructural transition is associated with the magnetic transion from (weak) ferromagnetic austenite to (weak) antiferromagnetic martensite. This ferromagnetic-antiferromagnetic phase transition obtained here from *ab initio*

csalculations has also recently been discussed in terms of an appropriate model Hamiltonian.[79]

With respect to martensitic transformations, the "structural exchange" parameters for tetragoonal and cubic states, J and K, in Eq. (8) are important. In addition, U_1 and the $U_{i,j}$ are magnetoelastic interaction constants. For a discussion of parameters related to Ni–Co–Mn–In alloys, see Ref. [80]. The Hamiltonian in Eq. (8) allows a first-order martensitic transformation with thermal hysteresis for a sufficiently large biquadratic elastic interaction, where we have chosen $0.2 < K/J < 0.37$.

Essentially, J and K and the remaining magnetoelastic interaction constants can be used to shift the martensitic transformation to make it coincide with the magnetic phase transition itself, see Ref. [80]. This then yields the large jump of the magnetization at the agnetocaloric phase transition as shown in Figure 1, where magnetism changes from (weak) ferromagnetism of austenite to (weak) antiferromagnetism of martensite.

Conflict of Interest

The authors declare no conflict of interest.

[1] T. Miyamoto, W. Ito, R. Y. Umetsu, R. Kainuma, T. Kanomata, K. Ishida, *Scr. Mater.* **2010**, *62*, 151.

[2] D. L. Schlagel, R. W. McCallum, T. A. Lograsso, *J. Alloys Compd.* **2008**, *463*, 38.

[3] W. M. Yuhasz, D. l. Schlagel, Q. Xing, K. W. Fennis, R. W. McCallum, T. A. Lograsso, *J. Appl. Phys.* **2009**, *105*, 07A921.

[4] W. M. Yuhasz, D. L. Schlagel, Q. XCing, R. W. McCallum, T. A. Lograsso, *J. Alloys Compd.* **2010**, *492*, 681.

[5] A. Çahır, M. Acet, M. Farle, *Sci. Rep.* **2016**, *6*, 28931.

[6] A. Çahır, M. Acet, *AIP Adv.* **2017**, *7*, 656424.

[7] T. Krenke, A. Çahır, F. Scheibel, M. Acet, M. Farle, *J. Appl. Phys.* **2016**, *120*, 243904.

[8] A. Çahır, M. Acet, U. Wiedwald, T. Krenke, M. Farle, *Acta Mater.* **2017**, *127*, 117.

[9] A. Backen, R. Niemann, S. Kaufmann, J. Buschbeck, L. Schultz, S. Fähler, ESOMAT 2009 – 8th European Symposium on Martensitic Transformations, Prague, Czech Republic. EDP Sciences, Les Ulis, France **2009**, p. 04002.

[10] D. Comtesse, M. E. Gruner, M. Ogura, V. V. Sokolovskiy, V. D. Buchelnikov, A. Grünebohm, R. Arróyave, N. Singh, T. Gottschall, O. Gutfleisch, V. A. Chernenko, F. Albertini, S. Fähler, P. Entel, *Phys. Rev. B* **2014**, *89*, 184403.

[11] J. M. Barandiaran, V. A. Chernenko, E. Cesari, D. Salas, P. Lapitza, J. Gutierrez, I. Oru, *Appl. Phys. Lett.* **2013**, *102*, 071904.

[12] J. M. Brandiaran, V. A. Chernenko, E. Cesari, D. Sala, J. Gutierrez, P. Lazpita, *J. Phys.: Condens. Matter* **2013**, *25*, 484005.

[13] G. Porcari, S. Fabbrici, F. Albertini, M. Buzzi, A. Paoluzi, J. Kamarad, Z. Arnold, M. Solzi, *Phys. Rev. B* **2012**, *85*, 024412.

[14] A. Planes, L. Mañosa, M. Acet, *J. Phys.: Condens. Matter* **2009**, *21*, 233201.

[15] V. V. Sokolovskiy, P. Entel, V. D. Buchelnikov, M. E. Gruner, *Phys. Rev. B* **2015**, *91*, 220409(R).

[16] R. Y. Umetsu, R. Kainuma, A. Amako, Y Taniguchi, T. Kanomata, K. Fukushima, A. Fujita, A. Oikawa, K. Ishida, *Appl. Phys. Lett.* **2008**, *93*, 042509.

[17] V. V. Khovaylo, T. Kanomata, T. Kanata, M. Nakashima, Y. Amako, R. Kainuma, R. Y. Umetsu, H. Morito, H. Miki, *Phys. Rev. B* **2009**, *80*, 144409.

[18] S. Chatterjee, S. Giri, S. K. De, S. Majumdar, *Phys. Rev. B* **2009**, *79*, 092410.

[19] J. I. Pérez-Landazabal, V. Recarte, V. Sanchez-Alarcos, C. Gómez-Polo, E. Cesari, *Appl. Phys. Lett.* **2013**, *102*, 101908.

[20] K. P. Bhatt, S. El-Khatib, V. Srivastava, R. D. James, C. Leighton, *Phys. Rev. B* **2012**, *85*, 134450.

[21] W. Ito, K. Ito, R. Y. Umetsu, R. Kainuma, K. Koyama, K. Watanabe, A. Fujita, K. Oikawa, K. Ishida, T. Kanomata, *Appl. Phys. Lett.* **2008**, *92*, 021908.

[22] X. Xu, W. Ito, R. Y. Umetsu, K. Koyama, R. Kainuma, K. Ishida, *Mater. Trans. JIM* **2010**, *51*, 469.

[23] A. Lakhani, S. Dash, A. Banerjee, P. Chaddah, X. Chen, R. V. Ramanjuan, *Appl. Phys. Lett.* **2011**, *99*, 242503.

[24] R. Y. Umetsu, K. Ito, W. Ito, K. Koyama, T. Kanomata, K. Ishida, R. Kainuma, *J. Alloys Compd.* **2011**, *509*, 1389.

[25] X. Xu, W. Ito, M. Tokunaga, R. Y. Umetsu, R. Kainuma, K. Ishida, *Mater. Trans. JIM* **2010**, *51*, 1357.

[26] X. Xu, W. Ito, M. Tokunaga, T. Kihara, K. Oka, R. Y. Umetsu, T. Kanomata, R. Kainuma, *Metals* **2013**, *3*, 298.

[27] S. K. Ghatak, D. K. Ray, *Phys. Rev. B* **1985**, *31*, 3064.

[28] D. K. Ray, J. P. Jordan, *Phys. Rev. B* **1986**, *33*, 5021.

[29] J. A. Monroe, J. E. Raymond, X. Xu, M. Nagasako, R. Kainuma, Y. I. Chumlyakov, R. Arroyave, I. Karaman, *Acta Mater.* **2015**, *101*, 107.

[30] T. Gottschall, K. P. Skokov, B. Frincu, O. Gutfleisch, *Appl. Phys. Lett.* **2015**, *106*, 021901.

[31] O. Mesheriakova, S. Chadow, A. K. Nayak, U. K. Rößler, J. Kübler, G. André, A. A. Tsirlin, J. Kiss, S. Hausdorf, A. Kalache, W. Schnelle, M. Nicklas, C. Felser, *Phys. Rev. Lett.* **2014**, *113*, 0897203.

[32] C. S. Mejia, A. K. Nayak, J. A. Schiemer, C. Felser, M. Nicklas, M. A. Carpenter, *J. Phys.: Condens. Matter* **2015**, *27*, 415402.

[33] S. Singh, S. W. D'Souza, J. Nayak, E. Suard, L. Chapon, A. Senyshyn, V. Petricek, Y. Skourskim, M. Nicklas, C. Felser, S. Chadov, *Nature Commun.* **2016**, *7*, 12671.

[34] C. Phatak, O. Heinonen, M. De Graef, A. Petford-Long, *Nano Lett.* **2016**, *16*, 4141.

[35] P. J. Webster, K. R. A. Ziebeck, S. L. Town, M. S. Peak, *Philos. Mag.* **1984**, *49*, 295.

[36] P. Entel, A. Dannenberg, M. Siewert, H. C. Herper, M. E. Gruner, V. D. Buchelnikov, V. A. Chernenko, *Mater. Sci. Forum* **2011**, *684*, 1.

[37] A. Çahır, L. Righi, F. Albertini, M. Acet, M. Farle, *Acta Mater.* **2015**, *99*, 140.

[38] P. Entel, V. D. Buchelnikov, V. V. Khovailo, A. T. Zayak, W. A. Adeagbo, M. E. Gruner, H. C. Herper, E. F. Wassermann, *J. Phys. D: Appl. Phys.* **2006**, *39*, 865.

[39] K. Ullakko, J. K. Huang, C. Kantner, R. C. O'Handley, V. V. Kokorin, *Appl. Phys. Lett.* **1996**, *69*, 1966.

[40] S. J. Murray, M. Marioni, S. M. Allen, R. C. O'Handley, *Appl. Phys. Lett.* **2000**, *77*, 886.

[41] O. Söderberg, Y. Ge, A. Sozinov, S.-P. Hannula, V. K. Lindroos, *Smart Mater. Struct.* **2005**, *14*, S223.

[42] B. Kiefer, D. C. Lagoudas, *Philos. Mag.* **2005**, *85*, 4289.

[43] I. Karaman, B. Basaran, H. E. Karaca, A. I. Karsilayan, Y. I. Chumlyakov, *Appl. Phys. Lett.* **2007**, *90*, 172505.

[44] S. Kaufmann, U. K. Rößler, O. Heczko, M. Wuttig, J. Buschbeck, L. Schultz, S. Fähler, *Phys. Rev. Lett.* **2010**, *104*, 145702.

[45] R. Niemann, U. K. Rößler, M. E. Gruner, O. Heczko, L. Schultz, S. Fähler, *Adv. Eng. Mater.* **2012**, *14*, 562.

[46] Y. Wang, C. Huang, J. Gso, S. Yang, . Ding, X. Song, X. Ren, *Appl. Phys. Lett.* **2012**, *101*, 101913.

[47] J. Liu, K. P. Gottschall, K. P. Skokov, J. D. Moore, O. Gutfleisch, *Nature Mater.* **2012**, *11*, 620.

[48] O. Pavlukhina, V. Sokolovskiy, V. Buchelnikov, P. Entel, *Mater. Sci. Forum* **2016**, *845*, 138.

[49] J. D. Kouvel, C. C. Hartelius, *J. Appl. Phys.* **1912**, *32*, 1343.

[50] S. A. Nikitin, G. Myalikgulyev, A. M. Tissin, M. P. Annaorazov, K. A. Asatryan, A. L. Tyurin, *Phys. Lett.* **1990**, *148*, 363.

[51] A. Chirkova, K. P. Skokov, L. Schultz, N. V. Baranov, O. Gutfleisch, T. Woodcock, *Acta Mater.* **2016**, *106*, 15.

[52] T. Zhou, M. K. Cher, L. Shen, J. F. Hou, Z. M. Yuan, *Phys. Lett. A* **2013**, *377*, 3052.

[53] M. Wolloch, M. E. Gruner, W. Keune, P. Mohn, J. Redinger, F. Hofer, D. Suress, R. Podloucky, J. Landers, S. Salamon, F. Scheibel, D. Spoddig, R. Witte, B. Roldan-Cuenya, O. Gutfleisch, M. Y. Hu, J. Zhao, T. Toellner, E. E. Alp, M. Siewert, P. Entel, R. Pentcheva, H. Wende, *Phys. Rev. B* **2016**, *94*, 174435.

[54] L. Sandratskii, Calculation with non-collinear spin-spiral method, unpublished data (2016).

[55] S. Mankovsky, Calculations with SPR-KKR, unpublished data (2016).

[56] X. Ren, Y. Wang, Y. Zhou, Z. Zhang, D. Wang, G. Fan, K. Otsuka, T. Suzuki, Y. Ji, J. Zhang, J. Tian, S. Hou, X. Ding, *Philos. Mag.* **2010**, *90*, 141.

[57] M. van Schilfgaarde, I. A. Abrikosov, B. Johansson, *Nature* **1999**, *400*, 46.

[58] A. Grüneboham, H. C. Herper, P. Entel, *J. Phys. D: Appl. Phys.* **2016**, *49*, 395001.

[59] I. Titov, M. Acet, D. González-Aloso, L. Mañosa, A. Planes, T. T. Krenke, *J. Appl. Phys.* **2012**, *112*, 073914.

[60] V. Recarte, J. I. Pérez-Landazábal, V. Sánchez-Alarcos, *J. Alloys Compd.* **2012**, *536*, S5308.

[61] D. Y. Cong, S. Roth, L. Schultz, *Acta Mater.* **2012**, *60*, 5335.

[62] E. Cesari, J. Font, J. Muntashell, P. Ochin, J. Pons, R. Santamarta, *Scr. Mater.* **2008**, *58*, 259.

[63] J. R. Aseguinolaqza, V. Colub, O. Y. Saluk, B. Muntifering, W. B. Knowlton, P. Müllner, J. M. Barandiaran, V. A. Cernenko, *Acta Mater.* **2016**, *111*, 194.

[64] D. Merida, J. A. Garćia, V. Sánchez-Aloarca, J. I. Perez-Landazábal, V. Recarte, F. Plazola, *J. Alloys Compd.* **2015**, *639*, 180.

[65] A. M. Pérez-Sierra, J. Pons, R. Santamarta, P. Vernaut, P. Ochin, *Acta Mater.* **2015**, *93*, 164.

[66] R. Kainuma, F. Geijima, Y. Sutou, I. Ohnuma, K. Aoko, K. Ishida, *Mater. Trans., JIM* **2000**, *41*, 943.

[67] R. W. Overholser, M. Wuttig, D. A. Neumann, *Scr. Mater.* **1999**, *40*, 1095.

[68] G. Kresse, J. Furthmüller, *Phys. Rev. B* **1996**, *54*, 11169. http://cms.mpi.uniVie.ac.at/VASP/

[69] J. S. Kaspar, J. S. Kouvel, *J. Phys. Chem. Solids* **1959**, *11*, 231.

[70] V. D. Buchelnikov, P. Entel, S. V. Taskaev, V. V. Sokolovskiy, A. Hucht, M. Ogura, H. Akai, M. E. Gruner, S. K. Nayak, *Phys. Rev. B* **2008**, *78*, 184427.

[71] V. D. Buchelnikov, V. V. Sokolovskiy, S. V. Taskaev, V. Khovaylo, A. A. Aliev, L. N. Khanov, A. B. Batadalov, P. Entel, H. Miki, T. Takagi, *J. Phys. D: Appl. Phys.* **2011**, *44*, 064012.

[72] V. V. Sokolovskiy, V. D. Buchelnikov, M. A. Zagrebin, P. Entel, S. Sahoo, M. Ogura, *Phys. Rev. B* **2013**, *87*, 019901.

[73] E. Vives, T. Castán, P. A. Lindgård, *Phys. Rev. B* **1996**, *53*, 8915.

[74] T. Castán, E. Vives, P. A. Lindgård, *Phys. Rev. B* **1999**, *60*, 7071.

[75] L. H. Bennett, V. Provenzano, R. D. Shull, I. Levin, E. Della Torre, Y. Jin, *J. Alloys Compd.* **2012**, *525*, 34.

[76] J. P. Perdew, K. Burke, M. Enzerhof, *Phys. Rev. Lett.* **1996**, *77*, 3865.

[77] The Munich SPR-KKR package, version 6.3, http://ebert.cup.uni-muenchen.de/SPRKKR; H. Ebert, D. Ködderitzsch, J. Minár, Rep. Prog. Phys. **2011**, *74*, 096501.

[78] A. I. Liechtenstein, M. I. Kaatnelson, V. P. Antropov, V. A. Gubanov, *J. Magn. Magn. Mater.* **1987**, *67*, 65.

[79] V. A. L'vov, E. Cesari, J. I. Pérez-Landazábal, V. Recarte, J. Torrens-Serra, *J. Phys. D: Appl. Phys.* **2016**, *49*, 095002.

[80] V. D. Buchelnikov, V. V. Sokolovskiy, M. A. Zagrebin, M. A. Tufatullina, P. Entel, *J. Phys. D: Appl. Phys.* **2015**, *48*, 164005.